Quadruple-Differentially-Driven Offset-Probe- Fed Patch Antenna for On-Antenna Power Combining

Timothee Le Gall, Anthony Ghiotto, Stefan Varault, Gwenaël Morvan, Bruno Louis, Gregoire Pillet

IEEE Access
Multidisciplinary | Rapid Review | Open Access Journal

Received 11 January 2024, accepted 21 January 2024, date of publication 29 January 2024, date of current version 6 February 2024.

Digital Object Identifier 10.1109/ACCESS.2024.3359438

RESEARCH ARTICLE

Quadruple-Differentially-Driven Offset-Probe-Fed Patch Antenna for On-Antenna Power Combining

TIMOTHÉE LE GALL[1], ANTHONY GHIOTTO[2], (Senior Member, IEEE), STEFAN VARAULT[1], GWENAËL MORVAN[1], BRUNO LOUIS[1], AND GREGOIRE PILLET[1]

[1]Thales DMS, 78990 Elancourt, France
[2]IMS Laboratory, Bordeaux INP, CNRS, University of Bordeaux, 33400 Talence, France

Corresponding author: Timothée Le Gall (timothee.legall@fr.thalesgroup.com)

ABSTRACT In this paper, a novel quadruple differentially driven offset probe fed patch antenna is introduced to extend the on-antenna power combining (OAPC) capabilities. This original design is based on the feeding of the two fundamental resonating modes of a square patch using offset differential probe pairs. Polarization diversity is obtained changing the relative phase difference between the differential driving signals. Using two orthogonally arranged offset differential pairs (each driving one of the two resonating modes), a four-port driven patch antenna (4DPA) is achieved. Then, mirror-duplicating the 4DPA feeding differential pairs (i.e., each resonating mode being then driven by two offset differential pairs), an eight-port driven patch antenna (8DPA) is obtained. For those structures, the offset probe pair common mode (CM) parasitic effect is studied. Then, mitigating technics based on the CM impedance control are introduced. One of them is implemented in 4DPA and 8DPA demonstrators using unbalanced commercial power amplifiers. Combining power directly into the antenna with up to eight ports in this work, improved efficiency, higher transmitted power, smaller associated monolithic microwave integrated circuits (MMIC) and enhanced heat dissipation are achieved compared to the alternative on-circuit power combining technics. As a proof of concept and to compare performance, passive and active demonstrators of reference one-port driven patch antennas (1DPA), 4DPAs and 8DPAs operating at 2.45 GHz are designed, fabricated and measured. The simulation and experimental results validate the proposed on-antenna combining technic, which is believed by the authors to be of particular interest to enhance performance of radar and communication silicon-based active antenna arrays.

INDEX TERMS Differentially-driven antennas, multi-port antennas, on-antenna power combining, patch antennas.

I. INTRODUCTION

Power amplifiers (PA) are essential components found in modern radar and communication systems. Significant work has been done over the recent years to improve output power, power added efficiency (PAE) and integrability. In particular, the GaAs and GaN III-V technologies have been the subject of considerable efforts. In [1], [2], and [3], very high output power, up to 10 W at X-band, was obtained using GaAs. However, the III-V technologies result in large chip size and high cost. Furthermore, their very low integrability (due to a small number of metal layers) impedes the co-integration of digital circuits. In fact, this matter is very critical as single-chip Tx/Rx modules are highly desired by the industry to meet stringent cost constraints, particularly for 5G beam-forming antenna arrays [4]. As a result, silicon technologies are at the forefront, especially the SiGe technologies which provide higher output power compared to the other silicon technologies, while maintaining a high integration capability. At X-band, in [5], a single-ended SiGe power amplifier deliv-

The associate editor coordinating the review of this manuscript and approving it for publication was Chan Hwang See.

ered up to 24.5 dBm. Meanwhile, in [6], [7], [8], and [9], up to 16 amplifiers are combined in-parallel to deliver up to 1 W of output power. However, compared to the GaAs technology, SiGe is far behind in terms of achievable saturated power (by about a decade at X-band). To mitigate this performance gap, it is essential to reduce SiGe on-circuit output power combiner losses and/or propose alternatives off-circuit power combining approaches. For instance, in [7], the insertion loss of the integrated 16-way output combiner is around 1.5 dB. In [9], the SiGe combining output balun results in an insertion loss of 0.75 to 2.2 dB in the 4.5 to 18 GHz frequency range. Suppressing these output losses would significantly improve the saturated power (P_{sat}) and the overall efficiency. Furthermore, the thermal dissipation at the circuit level will be decreased, resulting in lower stress on the transistors while enhancing their performance.

To benefit from the high level of integration of the SiGe technology while providing an enhanced output power, on-antenna power combining (OAPC) has emerged as a topic of interest. Its principle is illustrated in Fig. 1: rather than combining driving signals at the circuit level using lossy baluns and/or power combiners prior feeding a single-ended antenna, the signals are combined directly into the antenna using multiple access. Several types of multi-port antennas performing OAPC have been reported in the literature. In particular, this approach has been used for on-chip antenna designs operating at sub-THz frequencies, as OAPC is of high interest to improve the very limited output power of the TX modules. In [11], the on-chip antenna consists of a wideband ring antenna driven by eight signals, with a phase difference of 45° between each adjacent signal. The main advantage of this topology lies in its ability to be fed by an unlimited number of feeding points. However, only the circular polarizations can be achieved. In [12], a second sub-THz on-chip antenna based on a lens antenna fed by four pairs of differential amplifiers with an ultra-wideband behavior is presented. Yet, a lens of 12 mm in diameter is required, which makes the integration and fabrication highly difficult. In [13], off-chip OAPC at much lower frequencies (< 10 GHz) is introduced with up to three in-phase driving signals combined in a slot antenna. However, this configuration does not provide polarization diversity. Furthermore, its bandwidth is limited (~ 5 %). Alternatively, [13] introduces a symmetric geometry achieving polarization diversity. This design is based on a cavity-backed annular patch driven by two pairs of differential signals. Besides, in [15], [16], and [17], a patch antenna is fed by two double-fed slots resulting in a four-port antenna. In [18], a four-port probe-fed patch antenna, with polarization diversity, is presented. In [19], an eight-port configuration was proposed for the first time on printed circuit board (PCB) using stripline driven slots. However, this topology requires a complex stacking of substrates (> 4).

To significantly simplify the PCB stack (to 2 substrates) and ease the interconnection with an MMIC while maintaining the same OAPC capacity (8 ports), a polarization versatile quadruple-differentially-driven probe-fed (i.e., eight-port) patch antenna is introduced in this paper. Section II studies the common mode (CM) parasitic effect of the driving offset probe pairs with only two differential pairs first. Then, in section III, each pair is doubled, leading to an eight-port antenna. The inherent advantages of this antenna are discussed and highlighted, including polarization agility, filtering capability as well as reduced interconnection complexity with an MMIC. This last point is further elaborated in Section IV where mitigating interconnections between an MMIC and the multiport antenna is first proposed. A second interconnection is also discussed to provide a proof-of-concept with commercial off-the-shelf (COTS) components. In Section V, this technic is implemented in the fabrication of passive and active demonstrators, such as a four-port patch antenna (4DPA), and a eight-port patch antenna (8DPA). Simulation results obtained using CST Microwave Studio from Dassault Systems and experimental results are reported and compared to reference one-port driven patch antennas (1DPA) to validate the proposed OAPC technic. Finally, in Section VI, the proposed eight-port topology is compared to the state of the art and to a standard low-loss on-circuit power combining technic on PCB.

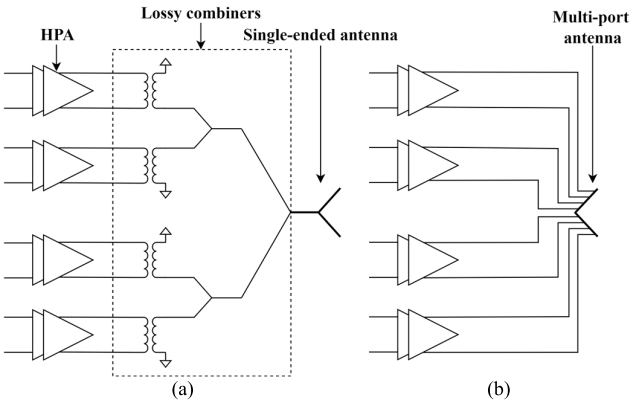

FIGURE 1. Illustration of (a) on-circuit power combining and (b) on-antenna power combining.

II. CM IMPEDANCE PARASITIC EFFECT ANALYSIS

The patch antenna is a well-known radiator. [20], [21], [22] present differentially-driven dual-polarized patches. Those designs implement two pairs of differential signals, (V_H^+, V_H^-) and (V_V^+, V_V^-), symmetrically arranged along the two orthogonal patch symmetrical axis. Each differential pair is coupled to a single resonating mode of the patch. Up to 90 dB of inter-port isolation is obtained.

Alternatively, in this paper, the feeding differential pairs, (V_H^+, V_H^-) and (V_V^+, V_V^-), are offset as illustrated in Fig. 3. Such offset implementation is inspired by the single driving pair implementation used in [23] to interconnect a balanced radio-frequency identification (RFID) chip to a single polarized patch antenna. In [24], a similar configuration is studied where a stack of patches is fed by four ports. Such multiport configuration filters the higher resonant modes compared to

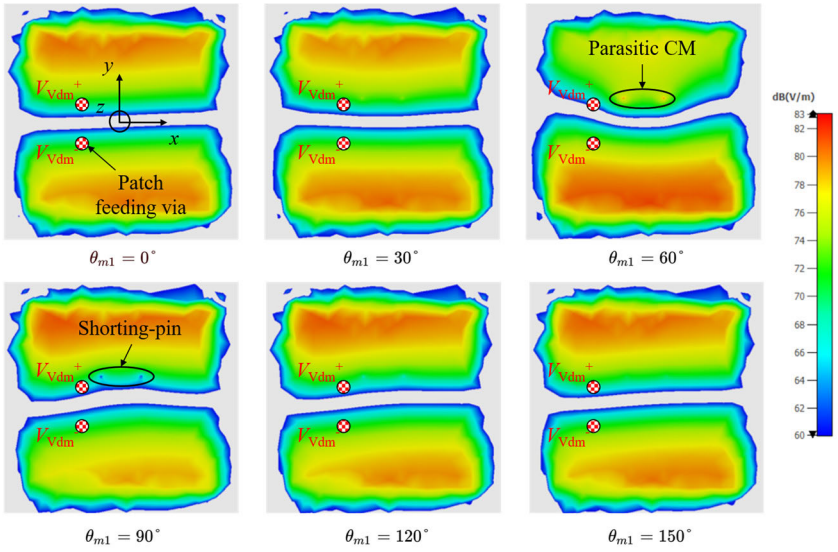

FIGURE 2. Perturbation on the TM_{01} mode E-field distribution at the resonant frequency versus the CM impedance of the V_H probe pair resulting from different interconnection electrical length θ_{m1}, with $\alpha_{m1} = 0$ dB, $Z_{cc1} = \infty\ \Omega$ and $\Delta l_x = 5$ mm.

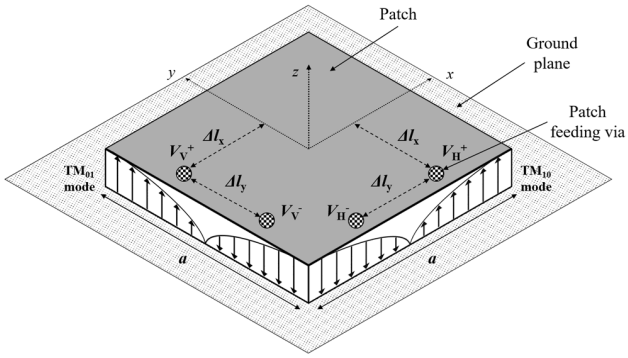

FIGURE 3. Illustration of the TM01 and TM10 modes inside a 4DPA fed by the (VV+, VV-) and (VH+, VH-) differential pairs, respectively.

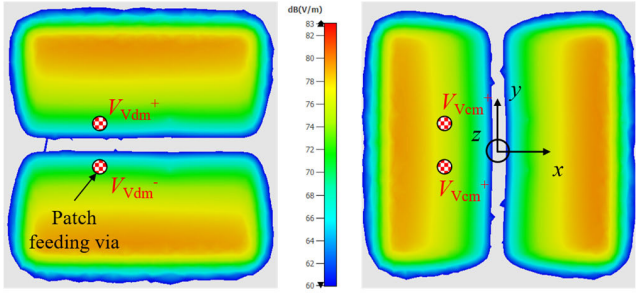

FIGURE 4. Simulated E-field magnitude of (a) the patch TM_{01} resonating mode stimulated by the DM of the (V_V^+, V_V^-) probe pair and (b) the patch TM_{10} resonating mode excited by the CM of the same probe pair.

this work. However, as highlighted in this paper, offsetting the feeding ports leads to a CM coupling with the patch resonating modes, occurring only when the two orthogonal modes are addressed. On one hand, Fig. 4(a) shows the excitation of the TM_{01} mode by the differential mode (DM) of the offset (V_V^+, V_V^-) pair, fed by two out of phase signals (V_{Vdm}^+, V_{Vdm}^-). On the other hand, in Fig. 4(b), the patch TM_{10} mode is excited by the CM of the same pair, fed by two in-phase signals (V_{Vcm}^+, V_{Vcm}^+). Therefore, in the dual-polarized configuration of Fig. 3, the DM of one of the two probe pair can couple to the CM of the other probe pair. Fig. 2 shows the E-field magnitude of the TM_{01} mode excited by the (V_V^+, V_V^-) DM and distorted by the CM impedance of the (V_H^+, V_H^-) probe pair. In this analysis, the configuration illustrated in Fig. 5 is considered. The square patch, etched on a Rogers 4003 substrate ($\varepsilon_r = 3.5$, $\tan\delta_d = 0.0027$) of thickness 1.524 mm, has a dimension $a = 31$ mm with a ground plane of 70×70 mm^2. The two driving pairs are offset by $\Delta l_x = 5$ mm. The probes of each pair are spaced by $\Delta l_y = 5$ mm. A differential port, port 2, is directly connected to the (V_V^+, V_V^-) probe pair. This port, as well as the other differential port, port 1, has DM and CM impedance $Z_{dd2} = Z_{dd1} = 100\ \Omega$ and $Z_{cc2} = Z_{cc1} = \infty\ \Omega$, respectively. To evaluate the interconnection effects, an ideal transmission line of electrical length θ_{m1} is cascaded in series with an ideal attenuator of attenuation value α_{m1} to connect the differential port 1 to the (V_H^+, V_H^-) probe pair. In Fig. 2, the effect of the CM impedance at the (V_H^+, V_H^-) probe pair plane obtained for various interconnection electrical length θ_{m1} can be observed (considering $\alpha_{m1} = 0$ dB). Significant distortion of TM_{01} mode is observed.

Therefore, particular attention must be paid in the feeding probe interconnection to ensure a high CM impedance. In the following parts, the interconnection electrical length and loss effects on the resonant frequency and efficiency are studied.

A. CM IMPEDANCE EFFECT ON THE RESONANCE FREQUENCY

Fig. 6 shows the TM_{01} mode resonance frequency versus the interconnection electrical length θ_{m1}, considering the circuit

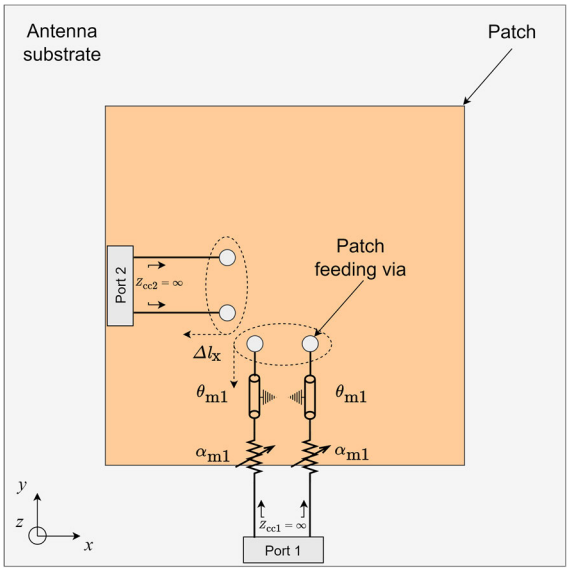

FIGURE 5. Studied configuration where the differential port 2 is directly connected to both ends (V_V^+, V_V^-) and port 1 is connected to (V_H^+, V_H^-) by uncoupled microstrips of electrical length θ_{m1} in series with attenuators of attenuation α_{m1}. The two probe pairs are simultaneously translated by Δl_x.

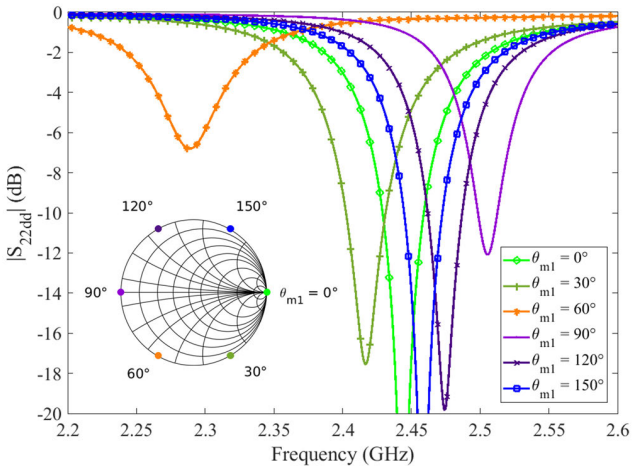

FIGURE 6. Reflection coefficient of the differential port 2 versus the port 1 microstrip feeding line electrical length θ_{m1} with $\alpha_{m1} = 0$ dB, $Z_{cc1} = \infty\ \Omega$ and $\Delta l_x = 4$ mm. The points on the Smith chart show the CM impedance at the (V_{H-}, V_{H+}) feeding probe pair plane for the corresponding θ_{m1} value.

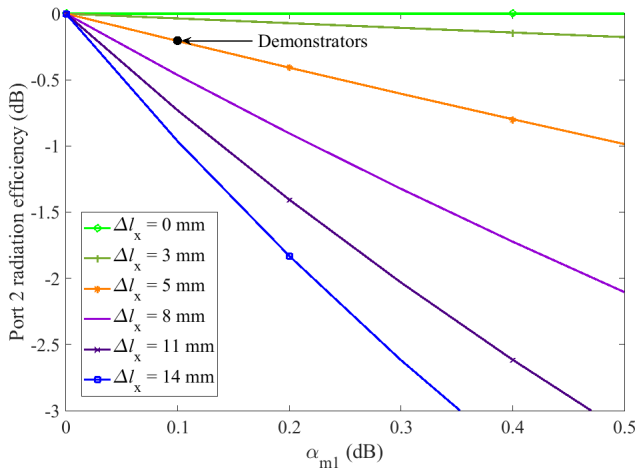

FIGURE 7. Simulated radiation efficiency obtained feeding the differential port 2 versus α_{m1} with $\theta_{m1} = 0°$ and $Z_{cc1} = \infty$ for different Δl_x translation values.

configuration shown in Fig. 5. It can be seen that the resonance frequency is shifted. This is due to the transformation of the CM open circuit found at the port 1 plane into another impedance value at the (V_H^+, V_H^-) feeding probe pair plane due to the interconnection electrical length θ_{m1}. For instance, a quarter wavelength interconnection ($\theta_{m1} = 90°$) transforms the CM open circuit at the port 1 plane into a short circuit at the (V_H^+, V_H^-) feeding probe pair plane to result in a shorted patch ([25], [26], [27]). The resulting CM impedance transformation for each variation of θ_{m1} is shown on the Smith chart in Fig. 6. This impedance transformation effect, with a good control of the interconnection, can be taken as an advantage to guarantee a high CM impedance to avoid CM coupling and frequency shifting.

B. CM IMPEDANCE IMPACT ON THE RADIATION EFFICIENCY

In the case $\Delta l_x = 0$ (i.e., the differential ports are located on the patch symmetrical axes), the probe pairs' CM cannot couple to the patch fundamental resonating modes. However, when the differential pairs are offset (as shown in Fig. 2), the differential signal from one port can couple to the CM of the other port. In the case $\theta_{m1} = 0°$ and $\alpha_{m1} = 0$ there is no coupling. However, considering interconnection losses ($\alpha_{m1} \neq 0$) the radiation efficiency is decreased depending on the CM coupling that depends on the Δl_x value. This behavior is illustrated in Fig. 7, considering $\theta_{m1} = 0°$, without conduction and dielectric losses. Again, the configuration shown in Fig. 5 is considered. Only the port 2 is excited with a differential signal. The simulated radiation efficiency was obtained by subtracting the directivity to the realized gain using the schematic tool from CST the higher the value of Δl_x, the stronger the coupling with the CM, thus the stronger the impact of the interconnection losses on the efficiency. For example, an attenuation of $\alpha_{m1} = 0.1$ dB, the radiation efficiency of port 2 decreases by 0.2 dB for $\Delta l_x = 5$ mm (attenuation and offset values of the demonstrators introduced in the following sections).

To conclude, the interconnection loss and Δl_x offset value must be minimized to optimize efficiency. This loss in efficiency should be put in regards to the combiner losses of an in-circuit combining approach to evaluate the advantage of the proposed OAPC technic. The comparison is drawn in section VI.

III. QUADRUPLE-DIFFERENTIALLY-DRIVEN PATCH FEEDING

The offset differential pairs (V_H^+, V_H^-) and (V_V^+, V_V^-) shown in Fig. 2, can be mirror-duplicated to obtain eight feeding points

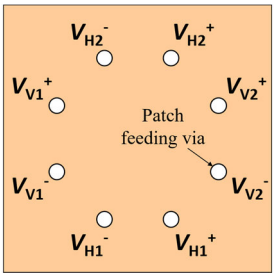

FIGURE 8. Illustration of the 8DPA, where the differential pairs (V_{V1}^+, V_{V1}^-) and (V_{V2}^+, V_{V2}^-) excite the vertical polarization whereas the other pairs feed the horizontal one.

TABLE 1. Phase difference for polarization agility.

	V_{V1-}	V_{V1+}	V_{V2-}	V_{V2+}	V_{H1-}	V_{H1+}	V_{H2-}	V_{H2+}
+45°	0°	180°	0°	180°	0°	180°	0°	180°
-45°	0°	180°	0°	180°	180°	0°	180°	0°
RHCP	0°	180°	0°	180°	90°	270°	90°	270°
LHCP	0°	180°	0°	180°	270°	90°	270°	90°
H	OFF	OFF	OFF	OFF	0°	180°	0°	180°
V	0°	180°	0°	180°	OFF	OFF	OFF	OFF

(four feeding points for each fundamental resonating mode). The resulting feeding topology, the 8DPA, is illustrated in Fig. 8. Such configuration has different advantages over the state of the art.

A. POLARIZATION AGILITY

The 8-port antenna can achieve all types of polarizations. Applying the proper relative amplitude and phase difference between the ((V_{H1}^+, V_{H1}^-) and (V_{H2}^+, V_{H2}^-)) and ((V_{V1}^+, V_{V1}^-) and (V_{V2}^+, V_{V2}^-)) set of feeding probe pairs (see Fig. 8 for ports location), all types of linear polarizations (LP), such as horizontal (H), vertical (V), slanted (+ and – 45°) and right-/left-handed circular (RHCP/LHCP) can be obtained (Table 1).

Simulated realized gains across each polarization - obtained by setting the corresponding phases and amplitudes of Table 1 - are reported in Fig. 9 to confirm the polarization agility of the proposed 8-port antenna. Very low axial ratio for the corresponding LHCP/RHCP is also shown in Fig. 10.

B. CHARACTERISTIC MODES ANALYSIS

Table 2 highlights the filtering capability of the proposed 8DPA compared to a single-ended patch antenna and the structure reported in [18].

The 8DPA filters five more resonant modes than the one-port version. Compared to the four-port version of [18], it achieves a better filtration capacity by removing the TM_{40} resonant mode. This characteristic would better help mitigate unwanted radiation at higher frequencies, especially due to the non-linearity characteristic of the amplifiers.

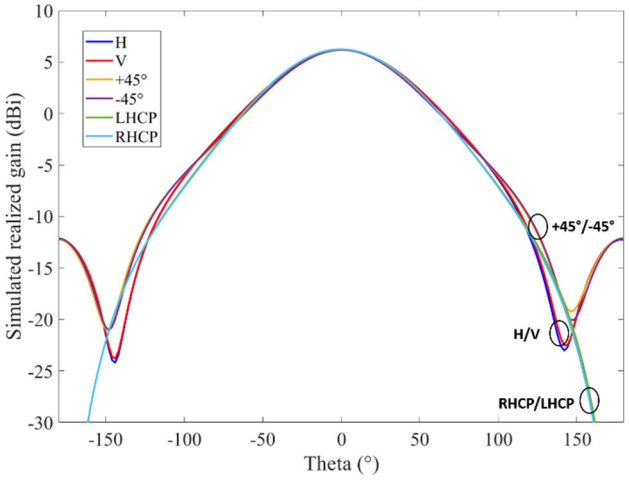

FIGURE 9. Simulated realized gain of the 8DPA with the phases and amplitudes of Table 1 to achieve each different polarization.

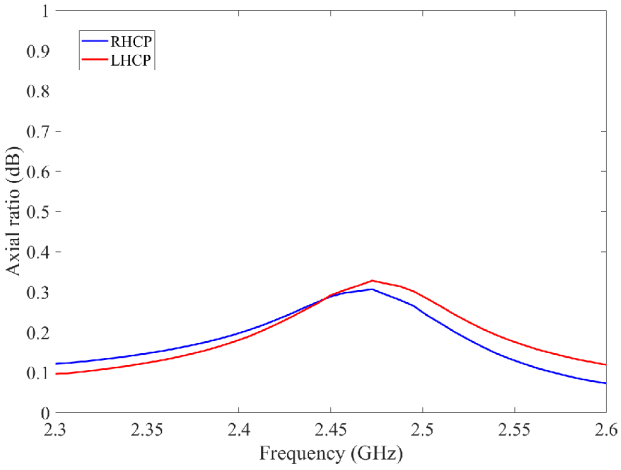

FIGURE 10. Simulated axial ratio of the 8DPA in LHCP and RHCP.

C. MMIC-TO-ANTENNA INTERCONNECTION EASE

In [18] and [19], in the perspective of integrating these multiport antennas with a dedicated MMIC, the interconnections would not be optimal. Considering a similar configuration than Fig. 11, i.e. with an MMIC placed on the back of the antenna, on an upper substrate, each end of the differential pairs are placed at two different sides of the MMIC. In a dual-polarized configuration, where the differential pair of each polarization are fed by one balanced amplifier, overlapping between the routing of each polarization is unavoidable, either inside the MMIC or on the multi-layer PCB through fan-out substrates. This increases the interconnection complexity and can result in additional losses. The proposed 8DPA solution avoids this possible overlap: each differential pair is placed on the same side of the MMIC. For instance, in Fig. 12, the differential pair (V_{H2}^+, V_{H2}^-) is placed only on the top of the figure. This allows a direct interconnection with the corresponding balanced amplifier and is of high interest

TABLE 2. Filtering capacity of different feeding topologies.

Demonstrator	Illustration	Frequency response	Higher modes
Single-ended antenna	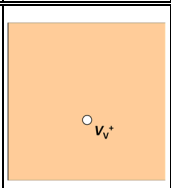	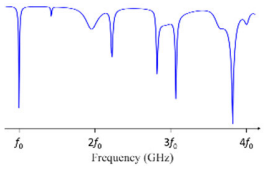	TM_{11} TM_{20} TM_{12} TM_{22} TM_{30} TM_{32} TM_{23} TM_{40}
Differential centered dual-polarized [18]	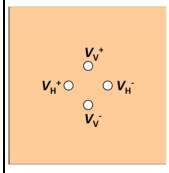	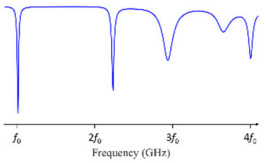	TM_{12} TM_{30} TM_{32} TM_{40}
Proposed 8DPA	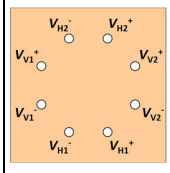	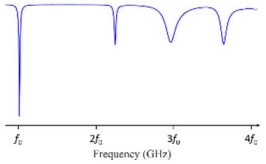	TM_{12} TM_{30} TM_{32}

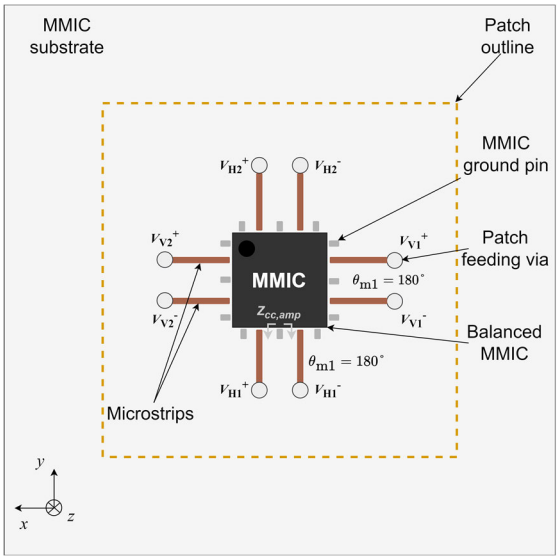

FIGURE 11. Illustration of the 8DPA, with the patch on an upper substrate, interconnected with a balanced output MMIC feeding both the horizontal (V_{H1}^+/V_{H1}^- and V_{H2}^+/V_{H2}^-) and vertical (V_{V1}^+/V_{V1}^- and V_{V2}^+/V_{V2}^-) polarization differential probe pairs.

for an implementation in active phased array, where size constraints and interconnection complexity are important.

D. BANDWIDTH ENHANCEMENT

Applications may require a large bandwidth, which is at odds with the proposed single-patch configuration. To extend the bandwidth, a parasitic patch can be implemented on the top of the first patch [28]. Fig. 12 shows a simulated wide bandwidth of 22 %, achieved by employing a foam-based substrate positioned between the previous bottom patch and the new upper patch. Nevertheless, designers should still be concerned about then electrical length of the interconnections between the MMIC and the proposed dual-patch configuration, as the resonance of the first patch can be shifted.

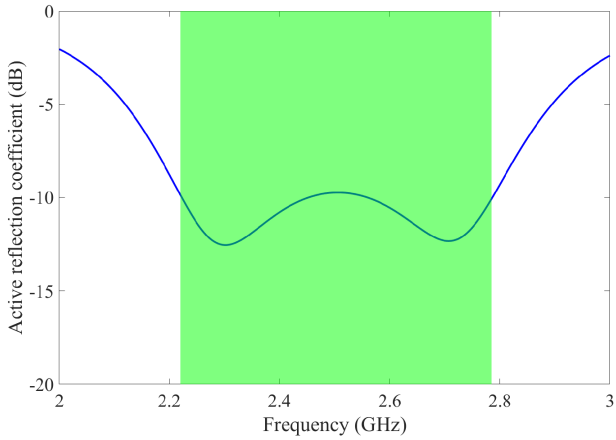

FIGURE 12. Simulated active reflection coefficient of the dual-patch 8-port antenna.

The above multiple advantages make the proposed antenna highly suitable for interconnection with an MMIC, compared to other feeding structures. The following section discusses the interconnections required to avoid the consequences of the CM coupling.

IV. MITIGATING INTERCONNECTION TECHNICS

In Fig. 11, a balanced output MMIC would be mounted on a top substrate, behind the radiating patch etched on the bottom copper layer of a bottom substrate. The horizontal polarization is fed by the two (V_{H1}^+, V_{H1}^-) and (V_{H2}^+, V_{H2}^-) pairs while the vertical one is fed by the (V_{V1}^+, V_{V1}^-) and (V_{V2}^+, V_{V2}^-) pairs. This structure, based on the proposed OAPC technic, is of great interest as it allows to transmit up to +9 dB of output power compared to a one-port driven antenna fed by a unique unbalanced amplifier. In addition, the differential pairs can be offset by any Δl_x value to comply with layout constraints without impacting their reflection coefficients, but possibly at the expense of a reduction in radiation efficiency due to CM effect, as introduced in the previous section. This feature lies in the fact that, for a constant Δl_y offset, the E-field magnitude is almost constant along the x-axis, as shown in Fig. 3(a).

Particular attention must be given to the patch feeding circuit. Two approaches are discussed in this section. The first one is based on the determination of the PA CM impedance and the co-design of the interconnection to obtain a high CM impedance at the feeding probe pair plane. The second consists in the implementation of a CM isolator with an appropriate interconnection electrical length guaranteeing a

high CM impedance at the feeding probe pair plane, independently of the interconnected active circuit.

A. CO-DESIGNED INTERCONNECTION

To properly interconnect a balanced output MMIC with the proposed multi-port antenna, it is essential to control the CM impedance at the probe plane, as discussed above. Therefore, a co-design approach considering the patch interconnection to guarantee a high CM impedance at the probe plane while minimizing the losses must be done. For instance, the integrated amplifier CM impedance $Z_{cc,amp}$ must be determined and transformed to a high impedance at the feeding probe plane using the proper interconnection circuit. In the case the active circuit present a CM open circuit at its output, this circuit simply consists in a $\theta_{m1} = 180°$ electrical length interconnection, as illustrated in Fig. 11.

At higher frequencies (> 20 GHz), advanced technologies such as high-density interconnect PCB or antenna-in-package (AiP) could be required to apply the proposed OAPC technic. In this paper, a different technique is employed to demonstrate the OAPC technic without involving a costly and time consuming dedicated MMIC design and fabrication.

B. INTERCONNECTION BASED ON A CM ISOLATOR

Alternatively, independently of the active circuit, a CM isolator can be implemented between the antenna feeding probes and the amplifiers. [29] reports a CM isolator based on slot lines. It provides a wideband and low-loss response (−0.4 dB at 2.45 GHz). The implemented slot line guarantees a CM open circuit ($Z_{cc} = \infty\ \Omega$) at the slot line plane. Its interconnection with a differential pair of the patch is realized by two microstrips of electrical length $\theta = 180°$ providing a CM open circuit at the feeding probe pairs. Fig. 13 illustrates the feeding of a 8DPA based on this CM isolator. Here a pseudo-differential configuration consisting of two out-of-phase unbalanced amplifiers is considered.

V. DEMONSTRATORS

For the proof of concept of the OAPC technic, passive and active PCB demonstrators implementing COTS components have been designed and fabricated. For ease of manufacturing and measurement, they all operate near 2.45 GHz. The second interconnection solution (presented above) is implemented in those demonstrators, for its simplicity, as the design is independent of the active circuit CM impedance. The size of the PCB feeding network implemented to divide the input signal can be significantly reduced implementing it at the MMIC level.

The schematic tool from CST Microwave Studio was used to perform co-simulations of active and passive components. This guarantees that the CM impedance of the amplifiers does not disturb the antenna performances thanks to the CM isolator.

For the 8DPA, the isolation between pairs exciting the same mode, for instance (V_{V1}^+, V_{V1}^-) and (V_{V2}^+, V_{V2}^-), is low and of the order of −10 dB. Therefore, the matching must now

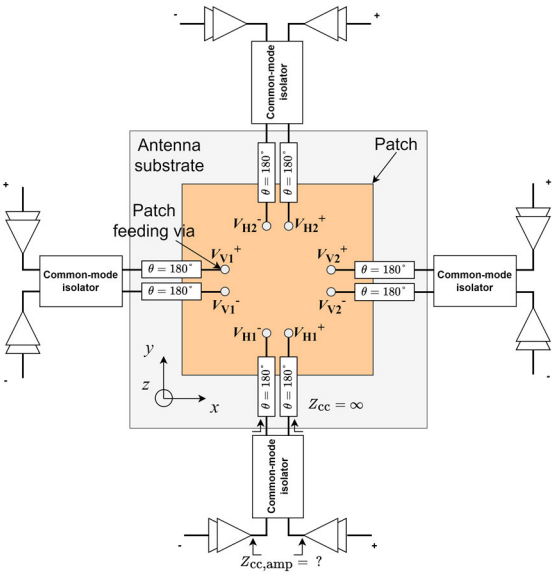

FIGURE 13. Illustration of the circuitry (CM isolators and 180° interconnections) required to properly feed the 8DPA using unbalanced amplifiers.

be analyzed through the active reflection coefficient (ARC) which considers the mutual coupling. The ARC is given by the following equation for the differential pair V_{V1}:

$$S_{V1V1,active} = S_{V1V1} + S_{V1V2}. \quad (1)$$

A. PASSIVE DEMONSTRATORS

For validation purpose, passive demonstrators of a reference 1DPA (Fig. 14), a 4DPA (Fig. 15) and an 8DPA (Fig. 16) operating near 2.45 GHz have been designed and fabricated. They all achieve a 45° slanted LP obtained exciting the four or eight feeding probes with relative phases corresponding to their + (0°) or – (−180°) suffixes (cf. Table 1). The prototypes are based on a multilayer PCB consisting of a top 1.524 mm thickness Rogers 4003 substrate implementing the radiating patch (Fig. 14(a), Fig. 15(a) and Fig. 16(a)) and a bottom 0.254 mm thickness Rogers 4350 substrate implementing the feeding circuits (Fig. 14(b), Fig. 15(b) and Fig. 16(b)). The two substrates are bounded by two layers of 0.101 mm thickness Rogers 4450F prepreg. All of the three square patches have a dimension a of 31 mm. Also, all of the demonstrators have the same ground plane dimension $L = 135$ mm. Each probe pair is offset by $\Delta l_x = 5$ mm and $\Delta l_y = 5$ mm. The antennas are fed by SMA connectors (located on the bottom left side of each circuit). Wilkinson dividers and 180°-hybrids, having 0.2 dB and 0.3 dB of loss at 2.45 GHz, respectively, are implemented in the 4DPA and 8DPA to drive all the feeding points with the appropriate phases and amplitudes to provide the desired 45° LP.

The slot-line-based CM isolators [29] are implemented in the ground plane between the two substrates. As highlighted in Fig. 13, the interconnections between the patch and the CM isolators were realized by meandered microstrip lines

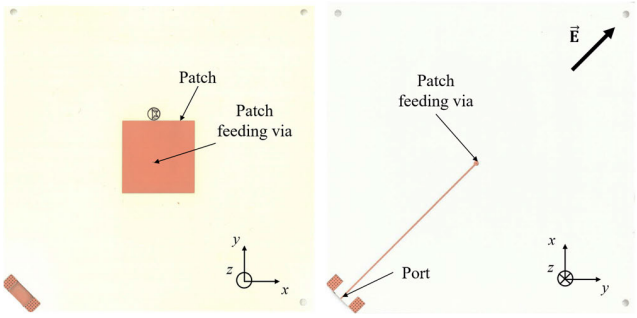

FIGURE 14. Photography of the passive 1DPA demonstrator: (a) top antenna side and (b) bottom circuit side.

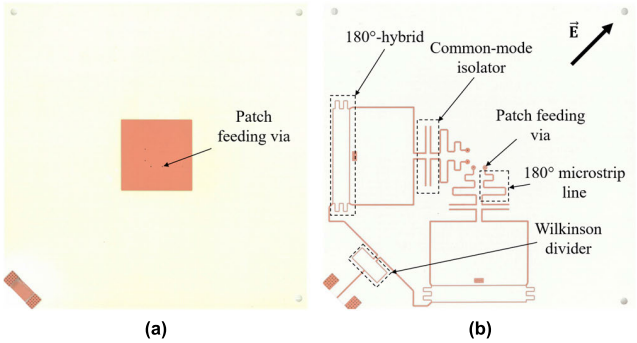

FIGURE 15. Photography of the passive 4DPA demonstrator: (a) top antenna side and (b) bottom circuit side.

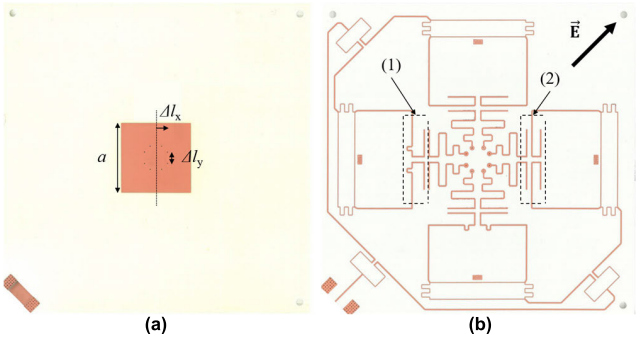

FIGURE 16. Photography of the passive 8DPA demonstrator: (a) top antenna side and (b) bottom circuit side where (1) and (2) show the microstrip phase compensation.

having an electrical length of $\theta = 180°$. In Fig. 16(b), it can be seen that the two pairs of a set ((V_{H1}^{+}, V_{H1}^{-}) and (V_{H2}^{+}, V_{H2}^{-})) or ((V_{V1}^{+},-V_{V1}^{-}) and (V_{V2}^{+}, V_{V2}^{-}))) are fed by two different CM isolator implementations, (1) and (2), providing (0°; −180°) and (−180°; 0°) output signals, respectively. This is done to provide the proper relative phases after the previous symmetrical divider stages, in order to achieve the desired 45° LP. (1) and (2) also have 0.4 dB of losses at 2.45 GHz.

The loss of each component is summarized in Table 3. The 180° transmission line, which interconnects the end of the slot-line to the antenna ports, has 0.1 dB of loss. This results in a CM parasitic loss of 0.2 dB, highlighted in Fig. 7.

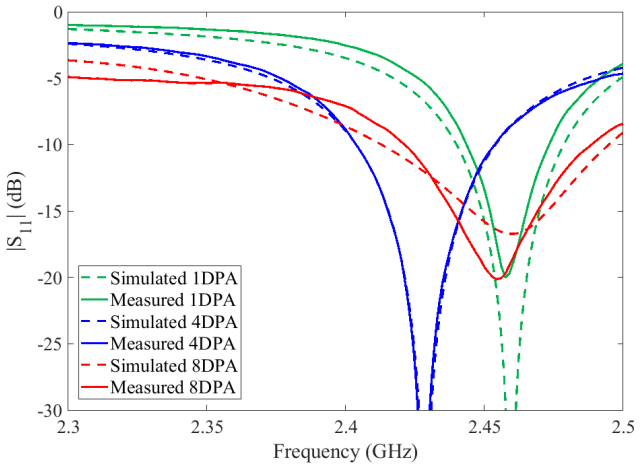

FIGURE 17. Simulated and measured reflection coefficients of the passive 1DPA, 4DPA and 8DPA demonstrators.

TABLE 3. Summary of the loss contributions found in the demonstrators feeding circuits.

Contributor	Loss (dB)
Wilkinson divider	0.2
180°-hybrid coupler	0.3
Common mode isolator	0.4
180° transmission line	0.1
CM parasitic effect	0.2

Fig. 17 shows the simulated and measured reflection coefficients of the passive 1DPA, 4DPA and 8DPA. A good correlation is obtained between the simulation and measurement results. Small discrepancy appears in the 8DPA demonstrator for which a slightly smaller bandwidth is obtained in measurement (probably due to fabrication tolerances). The bandwidth incremental increase (from the 1DPA to the 8DPA) is solely due to the feeding circuit losses: the OAPC has no effect on the bandwidth. The 1DPA, 4DPA and 8DPA are respectively centered at 2.46, 2.43 and 2.46 GHz. A small frequency shift of 1 % appears on the 4DPA due to its asymmetrical feeding. The radiation patterns were measured in an anechoic chamber at each demonstrator's resonant frequency. H-plane as well as E-plane co-polarization radiation patterns are plotted in Fig. 18.

Table 4 compares the measurement results of the three passive demonstrators. A very good agreement is found between simulation and measurement results.

Broadside, the gains are measured at 6.4, 5.5, and 5.0 dBi for the 1DPA, 4DPA and 8DPA, respectively. The gain can be improved using either a thicker and/or lower permittivity substrate. The gain differences are coherent considering the feeding circuit total losses obtained in simulation of the 1DPA (0.3 dB), 4DPA (1.4 dB) and 8DPA (1.8 dB) demonstrators (cf. Table 3 for details of the losses of each contribution –

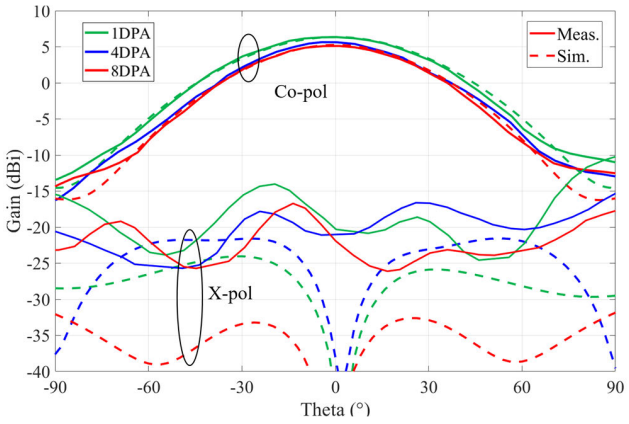

(a)

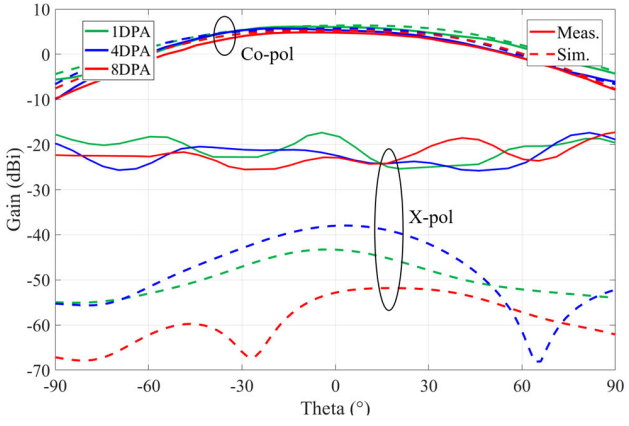

(b)

FIGURE 18. Simulated and measured radiation patterns of the passive demonstrators at their respective resonant frequency: (a) H-plane and (b) E-plane.

TABLE 4. Performance summary of the three passive demonstrators.

Demonstrator	Passive 1DPA	Passive 4DPA	Passive 8DPA
Resonant and measured frequency (GHz)	2.46	2.43	2.46
-10 dB bandwidth (MHz / %)	38 / 1.5	49 / 2	70 / 2.8
Measured gain (dBi)[#]	6.4	5.5	5
Measured normalized gain (dB)	0	-1.1	-1.4
Simulated efficiency (%)[*$]	80	80	79
Size (mm)	135 x 135	135 x 135	135 x 135

[#]Gain decrease with the number of ports due to the associated loss increase of the feeding circuits that are not part of the on-antenna power combining.
[*]Obtained from simulation at the patch feeding via reference plane.
[$]Takes into account the antenna efficiency and the combining efficiency

SMA connector not included) and the measurement uncertainties. The efficiency in Table 4 is obtained from simulation and given at the patch feeding via reference plane to effectively evaluate the OAPC technic efficiency. A constant efficiency of 80 % is achieved for the three configurations. This value is mostly due to the antenna substrate dielectric losses. Consequently, the constant efficiency implies that the on-antenna power combining technic is achieved without much loss, compared with standard power combining technics on PCBs or inside MMICs.

With respect to cross-polarization levels, the simulations show that the 8DPA achieves lower levels (about −10 dB at broadside) compared to the 1DPA and 4DPA, both in the E- and H-plane. This is an asset for the targeted AESA application for which low cross-polarization levels are desired.

The measurement setup available at the IMS research center was not optimized to allow the measurement of low levels of cross-polarization. This explains the differences between the simulation and the measurement results. Yet, the measured cross-polarization isolations are all better than 25 dB at broadside.

This experiment on passive demonstrators, especially the efficiency comparison, validates the OAPC technic introduced in this work. For further investigations, active demonstrators are presented in the following section with large signal measurements.

B. ACTIVE DEMONSTRATORS

1DPA, 4DPA and 8DPA active demonstrators operating at 2.45 GHz were fabricated (Fig. 19). The multilayer PCB assembly described in the previous section is again used. Unbalanced GVA-92+ PA from Minicircuits are implemented. In the 4DPA and 8DPA, the PAs are placed after the dividers, just before the CM isolators. Fig. 20 reports the large signal performance of a single GVA-92+. A small-signal gain of $G_{amp} = 15.4$ dB and an input compression point at 1 dB (ICP_1) of 10.3 dBm are obtained. In saturation, the GVA-92+ delivers an output power $P_{sat} = 26$ dBm and achieves a PAE of 45 %.

In principle, compared to the active 1DPA, a translation of the ICP_1 of +6 dB and +9 dB are expected for the active 4DPA and 8DPA, respectively. However, the losses of the dividing circuit of the demonstrators, upstream the PAs, must be considered, as they decrease the power available at the PAs input. Furthermore, as shown in Fig. 19, long microstrip lines are required to drive the signals, especially for the 8DPA, which further decrease the power available at the PAs input, and therefore, the ICP_1. Based on the dividing circuit losses, extra upstream PA losses of 0.6 dB and 1 dB are expected for the 4DPA and the 8DPA, respectively, compared to the 1DPA.

Therefore, ICP_1 translations of +6.6 dB and +10 dB are expected for the 4DPA and the 8DPA demonstrators, respectively, compared to the 1DPA demonstrator.

To measure the active demonstrators, a high-power setup measurement was used with a 2-port VNA (Fig. 21). An extra driver amplifier with a gain of +40 dB delivering up to 42 dBm was placed between the active antenna and the first VNA port to reach sufficient driving power to the GVA-92+ on the active antennas. The active antennas are placed on a motorized rotor driven by a real-time program running on a

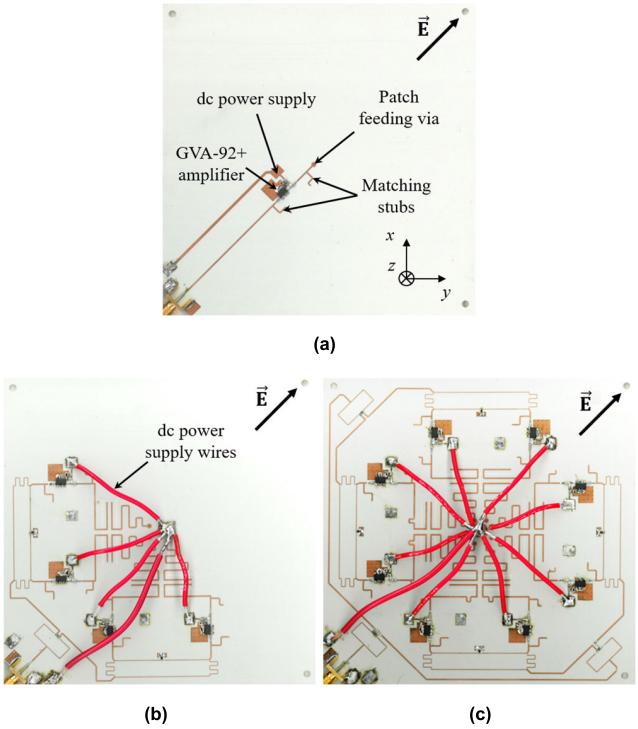

FIGURE 19. Bottom circuit side photography of the active (a) 1DPA, (b) 4DPA and (c) 8DPA demonstrators.

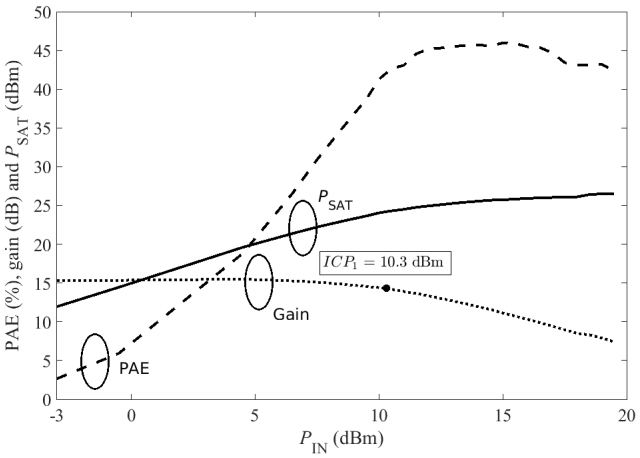

FIGURE 20. Large-signal characteristics measured at 2.45 GHz of the GVA-92+ amplifier implemented in the active demonstrators.

computer outside the anechoic chamber. It was also used for the passive demonstrators' radiation pattern measurements.

The second port of the VNA is connected to a calibrated Vivaldi antenna through a 5-meter SMA cable. Fig. 22 shows the results of the large-signal measurement carried out at broadside. Each gain was measured and normalized over the one of the passive 1DPA. The active antenna effective isotropic radiated power $EIRP_{AA}$ as well as the PAE_{AA}(corresponding to the power added efficiency of the active antenna including the on-antenna power combining impact) were calculated according to the following equations,

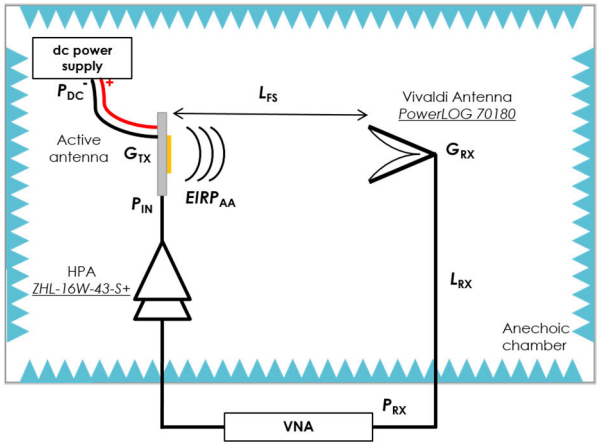

FIGURE 21. Large-signal measurement setup.

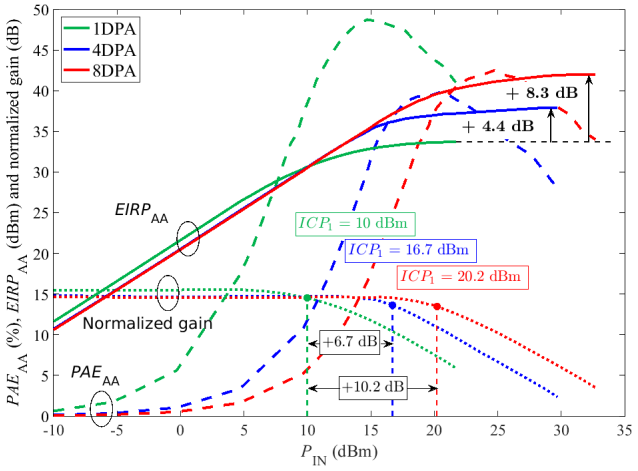

FIGURE 22. Non-linear characteristics, obtained at the respective resonant frequency, including the active antenna gain normalized over the passive 1DPA, the power-added efficiency and the EIRP of the active demonstrators.

extracted from the budget-link:

$$\mathrm{EIRP_{AA}} = P_{\mathrm{RX}} + L_{\mathrm{RX}} - G_{\mathrm{RX}} + L_{\mathrm{FS}}, \tag{2}$$

and

$$\mathrm{PAE_{AA}} = \frac{\mathrm{EIRP_{AA}} - G_{\mathrm{TX}} - P_{\mathrm{IN}}}{P_{\mathrm{DC}}}, \tag{3}$$

with P_{RX}, the power received by the second port of the VNA, L_{RX}, the 5-meter cable losses (−3.4 dB), G_{RX}, the Vivaldi antenna gain (8.3 dBi), L_{FS}, the free space losses calculated with an inter-antenna distance of 3.5 m, G_{TX}, the gain of the patch considered from the reference planes located just after the amplifiers, P_{IN}, the feeding power at the very input of the SMA plane of the active antenna and P_{DC}, the dc power consumption.

These two characteristics obtained by an over the air (OTA) measurement are considered since the power is combined on the antenna. (i.e., a conductive measurement is impossible). Losses from the 180° microstrip line, the CM isolator and

TABLE 5. Measured performance summary of the three active demonstrators.

Demonstrator	Active 1DPA	Active 4DPA	Active 8DPA
Resonant and measured frequency (GHz)	2.46	2.43	2.46
Gain* (dBi)	21.8	21.1	21
Normalized gain# (dB)	15.4	14.7	14.6
ICP_1 (dBm)	10	16.7	20.2
Normalized ICP_1 (dB)	0	6.7	10.2
$EIRP_{AA}$ (dBm)	34	38.4	42.3
Normalized $EIRP_{AA}$ (dB)	0	4.4	8.3
PAE_{AA} (%)	49	40	42
$P_{DC,MAX}$ (W)	0.85	3.3	6.6
Antenna size (mm x mm)	135 x 135	135 x 135	135 x 135

* absolute gain of the active antenna given at small signal
# gain normalized over the gain of the single-ended antenna (6.4dBi) in small signal

CM coupling (∼ 0.1, 0.4 dB and 0.2 dB, respectively) are included in both calculations because they are parts of the demonstrators. From Fig. 22, small and large-signal results can be analysed. Table 5 summarizes all the relevant values measured on the active prototypes, but also the gain and normalized gain of the previous passive prototypes.

Small-signal analysis: the active 1DPA provides a normalized gain (over the one of the passive 1DPA) of 15.4 dB which corroborates the conductive gain measurement of 15.4 dB (Fig. 20). The active 4DPA and 8DPA exhibit, respectively, a normalized gain of 14.7 dB and 14.6 dB. A small-signal gain decrease of 0.7 dB and 0.8 dB is then obtained for the active 4DPA and the active 8DPA, respectively, compared to the active 1DPA. For the 4DPA, this result is coherent with the passive demonstrator experiment for which a gain difference of 0.9 dB was obtained. However, a difference of 0.6 dB (0.8 vs 1.4 dB) occurs for the 8DPA when comparing the passive and active experiments. This difference may come from fabrication tolerances, antenna misalignment during the measurement and GVA-92+ discrepancies.

Large-signal analysis: the ICP_1 of the 1DPA is measured at 10 dBm, corroborating the conductive measurement result (10.3 dBm) taking into account the extra transmission line loss of the active 1DPA. The 4DPA ICP_1 is measured at +16.7 dBm which corroborates the expected translation of +6.6 dB compared to the 1DPA. The 8DPA reaches an ICP_1 value of 20.2 dBm. This value represents an improvement of +10.2 dB compared to the active 1DPA. This is again coherent with the expected value of +10 dB.

For the maximum $EIRP_{AA}$, again, in principle, improvements of +6 and +9 dB can be expected for the active 4DPA and 8DPA, respectively, compared to the active 1DPA. However, the 0.7 dB total loss downstream the amplifiers (0.4 dB loss of the CM isolator, 0.1 dB loss of the 180°-line and 0.2 dB loss of CM coupling losses (cf. II.b)), must be subtracted. This results in final expected improvements of +5.3 dB and +8.3 dB of $EIRP_{AA}$. Measurements show a +4.4 and +8.3 dB of improvement, respectively. Despite a poor correlation for the 4DPA (+4.4 vs +5.3 dB), a good correlation is found for the 8DPA (+8.3 vs +8.3 dB). Discrepancy reasons are discussed later.

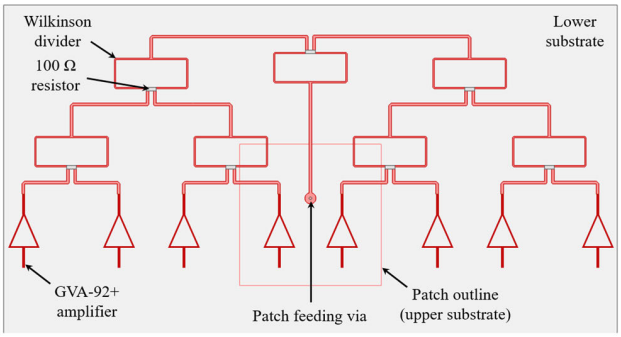

FIGURE 23. Illustration of on-circuit power combining using cascaded Wilkinsons prior to feeding a single-port patch antenna.

The maximum PAE_{AA} are measured at 49, 40 and 42 % respectively for the active 1DPA, 4DPA and 8DPA. A drop of about 8% of the 4DPA and 8DPA PAE compared to the 1DPA PAE is obtained. This is due to the 0.7 dB losses downstream of the PAs. They are causing a drop in both the output power and PAE. The PAE_{AA} of the 8DPA is slightly higher than the 4DPA one (+2 %). This may be due to OTA measurement uncertainties, including a slight tilt in the maximum gain radiation of the 4DPA, since it is not symmetrically fed, unlike the 8DPA. Other factors may come from the uncertainty of the demonstrators' manufacturing and the variability of GVA-92+ gain and large-signal performance. In addition, high current in dc resistive cables can cause a drop in the PA supply voltage. This effect decreases the PA performance. Another effect that can lead to a decrease in performance is the PAs heating which is well known to decrease the amplifiers' performance. With an MMIC co-design, some of these factors would be better controlled and the discrepancies would consequently be reduced.

The OAPC technic can be used in complement to in-circuit load modulated techniques such as the Doherty topology to further improve the back-off efficiency.

VI. COMPARISON

A. COMPARISON WITH PREVIOUS WORKS

Table 6 summarizes the state of the art of on-antenna power combining. The MMIC-to-antenna complexity (see IV.C) is only evaluated when the antenna achieves polarization agility. The introduced multi-port patch reaches eight feeding ports like the one presented in [19], allowing +9 dB of $EIRP_{AA}$ improvement compared to a single-driven version, but with a significantly lower number of substrates, and lower interconnection complexity. Compared to [18], the number of ports is doubled, the MMIC interconnection complexity is significantly reduced and higher filtering profile is obtained.

B. COMPARISON WITH ON-CIRCUIT POWER COMBINING

To thoroughly evaluate the on-antenna power combining technic, a comparison with a standard on-circuit power

TABLE 6. Comparison with previous on-antenna power combining works.

Ref.	Topology	Technology	Polarization states	Number of feeding points	$EIRP_{AA}$ improvement*	Minimum number of layers	Higher order modes filtering (up to $4f_0$)	MMIC-to-antenna interconnection complexity
[11]	Integrated ring	MMIC	2CP	8	+9 dB	-	-	-
[12]	Integrated lens	MMIC	4LP, 2CP	8	+9 dB	-	-	-
[13]	Slot	PCB	1LP	3	+4.77 dB	-	-	-
[14]	Cavity-backed annular patch	PCB	4LP, 2CP	4	+6 dB	2	-	Medium
[15]	Aperture-coupled patch	PCB	4LP, 2CP	4	+6 dB	4	-	High
[17]	Aperture-coupled patch	PCB	1LP	4	+6 dB	4	-	-
[24]	Probe-fed patch	PCB	1LP	4	+6 dB	2	All	-
[18]	Probe-fed patch	PCB	4LP, 2CP	4	+6 dB	2	[TM_{11}, TM_{20}, TM_{22}, TM_{23}, TM_{23}]	Medium
[19]	Aperture-coupled patch	PCB	4LP, 2CP	8	+9 dB	4	-	High
This work	**Probe-fed patch**	**PCB**	**4LP, 2CP**	**8**	+9 dB	**2**	**[TM_{11}, TM_{20}, TM_{22}, TM_{23}, TM_{23}, TM_{40}]**	**Low**

*Compared to a single-port antenna.

TABLE 7. Performance comparison between OCPC vs OAPC.

Technic	Post-amplifier losses (dB)
OCPC	-1
OAPC on PCB with CM isolators and associated 180° transmission lines	-0.7
OAPC with balanced MMIC and associated 180° transmission lines	-0.3

combining (OCPC) is performed. Fig. 23 shows the combiner used. Eight amplifiers are placed in parallel, like the 8DPA, but are combined by low loss Wilkinson dividers before feeding a single-ended patch antenna through a via, as in the previous demonstrators. The Wilkinson dividers are the same as the ones used previously, which have been optimized at 2.45 GHz, on a 0.254 mm Rogers 4350 substrate. Table 7 compares the losses of the OAPC technic to the simulated OCPC technic. The OAPC technic used for the 8DPA demonstrators (including the CM isolators and 180° transmission lines) achieves lower losses than a regular 8-to-1 low-loss on-circuit combiner. With an MMIC interconnection, the OAPC could achieve even lower losses by removing the CM isolators since a balanced amplifier would provide the common-mode impedance condition.

VII. CONCLUSION

In this paper, a quadruple-differentially-driven probe-fed patch antenna is introduced. In this structure, the two fundamental modes of a square patch are fed independently by two offset differential pairs. Compared to a one-port driven antenna, the proposed 8-port antenna achieves up to +9 dB of radiated power. Compared to the state of the art, it also achieves polarization agility, higher mode filtering, reduced interconnection complexity as well as ease of fabrication by minimizing the substrates used. In addition, a parasitic patch can be implemented to widen the bandwidth.

This structure is believed by the authors to be of high interest for active antenna arrays based on silicon MMICs used in radar and communication applications to enhance the radiated power.

REFERENCES

[1] C.-K. Chu, H.-K. Huang, H.-Z. Liu, C.-H. Lin, C.-H. Chang, C.-L. Wu, C.-S. Chang, and Y.-H. Wang, "A 9.1–10.7 GHz 10-W, 40-dB gain four-stage PHEMT MMIC power amplifier," *IEEE Microw. Wireless Compon. Lett.*, vol. 17, no. 2, pp. 151–153, Feb. 2007.

[2] A. P. de Hek, P. A. H. Hunneman, M. Demmler, and A. Hulsmann, "A compact broadband high efficient X-band 9-watt PHEMT MMIC highpower amplifier for phased array radar applications," in *IEEE GaAs IC Symp. Dig.*, Oct. 1999, pp. 276–280.

[3] W. Bosch, J. G. E. Mayock, M. F. O'Keefe, and J. McMonagle, "Low cost X-band power amplifier MMIC fabricated on a 0.25 μm GaAs PHEMT process," in *Proc. IEEE Int. Radar Conf.*, Sep. 2005, pp. 22–26.

[4] I. Syrytsin, S. Zhang, G. F. Pedersen, and A. S. Morris, "Compact quad-mode planar phased array with wideband for 5G mobile terminals," *IEEE Trans. Antennas Propag.*, vol. 66, no. 9, pp. 4648–4657, Sep. 2018.

[5] Y. S. Noh, M. S. Uhm, and I. B. Yom, "A compact Ku-band SiGe power amplifier MMIC with on-chip active biasing," *IEEE Microw. Wireless Compon. Lett.*, vol. 20, no. 6, pp. 349–351, Jun. 2010.

[6] C. Liu, Q. Li, Y. Li, X.-D. Deng, X. Li, H. Liu, and Y.-Z. Xiong, "A fully integrated X-band phased-array transceiver in 0.13-μm SiGe BiCMOS technology," *IEEE Trans. Microw. Theory Techn.*, vol. 64, no. 2, pp. 575–584, Feb. 2016.

[7] Y. Chen, M. P. van der Heijden, and D. M. W. Leenaerts, "A 1-Watt Ku-band power amplifier in SiGe with 37.5% PAE," in *Proc. IEEE Radio Freq. Integr. Circuits Symp. (RFIC)*, May 2016, pp. 324–325.

[8] J. Andrews, "An 850 mW X-band SiGe power amplifier," in *Proc. IEEE BCTM*, Oct. 2008, pp. 109–112.

[9] C. Liu, Q. Li, Y. Li, X. Li, H. Liu, and Y.-Z. Xiong, "An 890 mW stacked power amplifier using SiGe HBTs for X-band multifunctional chips," in *Proc. ESSCIRC Conf. 41st Eur. Solid-State Circuits Conf. (ESSCIRC)*, Sep. 2015, pp. 68–71.

[10] E. Kerherve, N. Demirel, A. Ghiotto, A. Larie, N. Deltimple, J.-M. Pham, Y. Mancuso, and P. Garrec, "A broadband 4.5–15.5-GHz SiGe power amplifier with 25.5-dBm peak saturated output power and 28.7% maximum PAE," *IEEE Trans. Microw. Theory Techn.*, vol. 63, no. 5, pp. 1621–1632, May 2015.

[11] S. M. Bowers and A. Hajimiri, "Multi-port driven radiators," *IEEE Trans. Microw. Theory Techn.*, vol. 61, no. 12, pp. 4428–4441, Dec. 2013.

[12] B. Goettel, P. Pahl, C. Kutschker, S. Malz, U. R. Pfeiffer, and T. Zwick, "Active multiple feed on-chip antennas with efficient in-antenna power combining operating at 200–320 GHz," *IEEE Trans. Antennas Propag.*, vol. 65, no. 2, pp. 416–423, Feb. 2017.

[13] T. Chi, S. Li, J. S. Park, and H. Wang, "A multifeed antenna for high-efficiency on-antenna power combining," *IEEE Trans. Antennas Propag.*, vol. 65, no. 12, pp. 6937–6951, Dec. 2017.

[14] M. Manteghi and Y. Rahmat-Samii, "Multiport characteristics of a wide-band cavity backed annular patch antenna for multipolarization operations," *IEEE Trans. Antennas Propag.*, vol. 53, no. 1, pp. 466–474, Jan. 2005.
[15] D. M. Pozar and S. M. Duffy, "A dual-band circularly polarized aperture-coupled stacked microstrip antenna for global positioning satellite," *IEEE Trans. Antennas Propag.*, vol. 45, no. 11, pp. 1618–1625, Nov. 1997.
[16] S. D. Targonski and D. M. Pozar, "Design of wideband circularly polarized aperture-coupled microstrip antennas," *IEEE Trans. Antennas Propag.*, vol. 41, no. 2, pp. 214–220, Feb. 1993.
[17] T. Le Gall, A. Ghiotto, S. Varault, G. Morvan, B. Louis, and G. Pillet, "Quadruple-fed aperture-coupled microstrip patch antenna for on-antenna power combining," in *Proc. 51st Eur. Microw. Conf. (EuMC)*, Apr. 2022, pp. 55–58.
[18] W. Duan, X. Y. Zhang, S. Liao, K. X. Wang, and Q. Xue, "Multiport power combining patch antenna with stable reflection coefficient and radiation pattern in six polarization states," *IEEE Trans. Antennas Propag.*, vol. 67, no. 2, pp. 719–729, Feb. 2019.
[19] T. Le Gall, A. Ghiotto, S. Varault, G. Morvan, B. Louis, and G. Pillet, "Wideband quadruple-differentially-fed aperture-coupled stacked patch antenna," in *Proc. 52nd Eur. Microw. Conf. (EuMC)*, Sep. 2022, pp. 167–170.
[20] H. Nawaz and I. Tekin, "Double-Differential-fed, dual-polarized patch antenna with 90 dB interport RF isolation for a 2.4 GHz in-band full-duplex transceiver," *IEEE Antennas Wireless Propag. Lett.*, vol. 17, pp. 287–290, 2018.
[21] N.-W. Liu, L. Zhu, X. Zhang, and W.-W. Choi, "A wideband differential-fed dual-polarized microstrip antenna under radiation of dual improved odd-order resonant modes," *IEEE Access*, vol. 5, pp. 23672–23680, 2017.
[22] H. H. Bae, T. H. Jang, H. Y. Kim, and C. S. Park, "Broadband 120 GHz L-probe differential feed dual-polarized patch antenna with soft surface," *IEEE Trans. Antennas Propag.*, vol. 69, no. 10, pp. 6185–6195, Oct. 2021.
[23] A. Ghiotto, S. F. Cantalice, T. P. Vuong, A. Pouzin, G. Fontgalland, and S. Tedjini, "Miniaturized patch antenna for the radio frequency identification of metallic objects," in *IEEE MTT-S Int. Microw. Symp. Dig.*, Jun. 2008, pp. 583–586.
[24] F. Huang, L. Zhu, and H. Zhang, "Study on a multi-point differential feeding strategy for design of filtering patch antennas with stopband enhancement," *IEEE Trans. Antennas Propag.*, vol. 70, no. 12, pp. 11293–11300, Dec. 2022.
[25] D. Schaubert, F. Farrar, A. Sindoris, and S. Hayes, "Microstrip antennas with frequency agility and polarization diversity," *IEEE Trans. Antennas Propag.*, vol. AP-29, no. 1, pp. 118–123, Jan. 1981.
[26] X. Zhang and L. Zhu, "Gain-enhanced patch antennas with loading of shorting pins," *IEEE Trans. Antennas Propag.*, vol. 64, no. 8, pp. 3310–3318, Aug. 2016.
[27] X. Zhang and L. Zhu, "High-gain circularly polarized microstrip patch antenna with loading of shorting pins," *IEEE Trans. Antennas Propag.*, vol. 64, no. 6, pp. 2172–2178, Jun. 2016.
[28] R. B. Waterhouse, "Design of probe-fed stacked patches," *IEEE Trans. Antennas Propag.*, vol. 47, no. 12, pp. 1780–1784, Dec. 1999.
[29] T. L. Gall, A. Ghiotto, S. Varault, B. Louis, and G. Pillet, "Ultra-low loss slot-line based common mode isolator," in *Proc. 53rd Eur. Microw. Conf. (EuMC)*, Sep. 2023, pp. 58–61.

TIMOTHÉE LE GALL received the M.S. degree in electronics and microwaves from Institut National Polytechnique de Bordeaux (ENSEIRB-MATMECA), Bordeaux, France, in 2019, and the Ph.D. degree from the University of Bordeaux, in 2023. He did his Ph.D. thesis with Thales Defence Mission Systems, Elancourt, France, where he is currently a Research Engineer. His current research interests include RCS reduction techniques, electromagnetic absorbers, and antenna arrays.

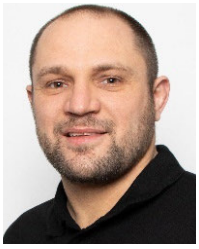

ANTHONY GHIOTTO (Senior Member, IEEE) received the M.Sc. and Ph.D. degrees (Hons.) in optics, optoelectronics, and microwave engineering from the Grenoble Institute of Technology, Grenoble, France, in 2005 and 2008, respectively.

From 2009 to 2012, he was a Postdoctoral Research Associate with École Polytechnique de Montréal, Montréal, QC, Canada. In 2012, he joined the Department of Electronics, ENSEIRB-MATMECA Engineering School, Bordeaux Institute of Technology, and the Laboratory of Integration from Materials to Systems (IMS), University of Bordeaux, where he is currently an Associate Professor [with Full Professor (Habilitation)]. In 2016 and 2017, he has been a Guest Professor with the University of Pavia, Pavia, Italy. He was a recipient of the IEEE MTT-S Outstanding Young Engineer Award, in 2022, the IEEE/SEE Léon-Nicolas Brillouin Award, in 2020, the IEEE SPI Young Investigator Training Program Award, in 2016 and 2017, the Postdoctoral Fellowship from the Merit Scholarship Program for Foreign Students of Fonds Québécois de la Recherche sur la Nature et les Technologies of Québec, in 2009, and the Young Scientist Award of the International Union of Radio Science, in 2008. His current research interests include the analysis, design and integration of microwave and millimeter wave passive and active circuits in PCB (including SIW and Air-Filled SIW), dielectric waveguides, and BiCMOS and CMOS technologies. He is the 2024 IEEE MTT-S Adcom Secretary. He was the TPC Chair of the 2019 European Microwave Conference (EuMC) and will be the Chair of the 2024 European Microwave Conference (EuMC). He is also an Associate Editor of the *EuMA International Journal of Microwave and Wireless Technologies* and a Technical Reviewer of IEEE TRANSACTIONS ON MICROWAVE THEORY AND TECHNIQUES, IEEE TRANSACTIONS ON ANTENNA AND PROPAGATION, IEEE MICROWAVE AND WIRELESS COMPONENTS LETTERS, and the IEEE ANTENNAS AND WIRELESS PROPAGATION LETTERS. He is the Chair of the MTT-4 Microwave Passive Components and Transmission Line Structures and a member of the MTT Technical Coordination and Future Directions Committee (TCFDC), the MTT-1 Field Theory and Computational EM, and the MTT-5 Filters Committees of the IEEE Microwave Theory and Technique Society (MTT-S). Since 2017, he has been the Chair of the IEEE MTT French Chapter. He was the Counselor of the IEEE Student Branch of Bordeaux: The BEE Branch, from 2012 to 2019, and is an Advisor of the MTT and AP BEE Branch Chapters.

STEFAN VARAULT received the M.S. degree in electronics, optoelectronics, and microwaves from Institut National Polytechnique de Toulouse (ENSEEIHT), Toulouse, France, in 2007, and the Ph.D. degree from Université Paul Sabatier of Toulouse, Toulouse, in 2011. He did his Ph.D. thesis with ONERA, Toulouse. He held a post-doctoral research position with Institut Fresnel, Marseille, France. In 2013, he joined Télécom ParisTech, Paris, France, for a two-year contract. He is currently a Research Engineer with Thales Defence Mission Systems, Elancourt, France. His current research interests include frequency selective structures and metamaterials, tunable/reconfigurable structures, wideband antennas and antenna arrays, electromagnetic absorbers, and RCS reduction techniques.

GWENAËL MORVAN received the M.S. degree in electronics and microwave from Université de Bretagne Occidentale (UBO), Brest, France, in 1993, and the Diplôme Universitaire (DU) degree in astrophysics (M1) from Observatoire de Paris/Meudon (OBSPM), Fenêtre sur l'Univers, France, in 2014. Between 1994 and 2000, he did his Ph.D. thesis with Laboratoire d'Electronique et Systèmes de Télécommunication (LEST) and École Nationale Supérieure des Télecommunication (ENST), Brest. In 2000, he joined Thales, Elancourt, France. He is currently a Design Engineer with Thales Defense Mission System (DMS), Elancourt. His current interests include antenna arrays, wideband antennas, RCS reduction techniques, reflect arrays, slot antennas, and AI applied to electromagnetic.

BRUNO LOUIS received the Dipl.-Ing. degree from École Nationale Supérieure d'Ingénieurs de Caen-Institut des Sciences de la Matière et du Rayonnement, France, in 1989. In 1990, he joined Thales Defence Mission Systems, Elancourt, France. He is currently lead analog & RF ASIC design and in charge of developments of transmit/receive (T/R) modules in silicon technology.

GREGOIRE PILLET received the M.S. degree in laser-matter interactions physics from École Polytechnique, France, in 2007, the degree from École Nationale Supérieure des Télécommunication, France, in 2007, and the Ph.D. degree from École Polytechnique, in 2013. He is currently with Thales Defence Mission Systems, France. His research interests include LiDAR systems, microwave photonics, antennas, low observable technologies, and radar and electronic warfare systems.